

1 **An Integrated Kinematic and Geochemical Model to Determine Lithospheric**
2 **Extension and Mantle Temperature from Syn-Rift Volcanic Compositions**

3 S.M. Dean^a, B.J. Murton^a, T.A. Minshull^a, T.J. Henstock^a and R.S. White^b

4 ^a National Oceanography Centre, University of Southampton, Southampton, SO14
5 3ZH, United Kingdom

6 ^b Bullard Laboratories, Department of Earth Sciences, University of Cambridge,
7 Cambridge, CB3 0EZ, United Kingdom

8 **E-mail Addresses:** smd9@noc.soton.ac.uk (S.M. Dean), bjm@noc.soton.ac.uk (B.J.
9 Murton), tmin@noc.soton.ac.uk (T.A. Minshull), then@noc.soton.ac.uk (T.J.
10 Henstock), rwhite@esc.cam.ac.uk (R.S. White).

11 **Corresponding Author:** S.M. Dean; National Oceanography Centre, University of
12 Southampton, Southampton, SO14 3ZH, United Kingdom; smd9@noc.soton.ac.uk;
13 Tel.: +44 (0)2380 592260; fax: +44 (0)2380 593052.

14 **Abstract**

15 We present an integrated kinematic and geochemical model that determines the
16 composition of melts and their residual source rocks generated by decompression
17 melting of the mantle during continental rifting. Our approach is to construct a unified
18 numerical solution that merges an established lithospheric stretching model which
19 determines the rate and depth at which melting occurs, with several compositional
20 parameterisations of mantle melting to predict the composition of primary melts. We
21 also incorporate a parameterisation for the rare earth elements. Using our approach,
22 we are able to track the composition of the melt fractions and mantle residues as
23 melting progresses. Our unified model shows that primary melt composition is

24 sensitive to rift duration and mantle temperature, with rapid rifting and higher mantle
25 temperatures producing larger melt fractions, at a greater mean pressure of melting,
26 than slower/cooler rifting. Comparison of the model results with primitive basalts
27 recovered from oceanic spreading ridges and rifted margins in the North Atlantic
28 indicates that rift duration and synrift mantle temperature can be inferred
29 independently from the appropriate geochemical data.

30 **Keywords:** melt composition; continental margin; rifting

31 **1. Introduction**

32 Melting of the mantle occurs at rifted continental margins in response to
33 decompression as mantle rocks are brought toward the surface by lithospheric
34 extension. This melting is controlled by several parameters including: the initial
35 mantle temperature and source composition; the rate of continental extension; the
36 final degree of lithospheric stretching (β_{max}); and the initial lithospheric thickness [1].
37 Several studies have attempted to estimate some of these parameters from estimates of
38 rift-related magmatic volume (e.g., [2],[3],[4],[5],[6]). This volume is usually
39 estimated from wide-angle seismic data. Igneous products, added to the lower crust
40 (i.e., underplated or intruded complexes) are identified as regions of high seismic
41 velocity [2] relative to normal continental crust (e.g., [7]). Extrusive volcanics (i.e.,
42 flood basalts) are identified as high amplitude seaward dipping reflector sequences on
43 the continent-ocean transition. Examples of both intrusive and extrusive magmatic
44 rocks are found on “volcanic” margins such as the East Greenland margin [5],[8] the
45 Faeroes margin and Hatton Bank [9]. In contrast, such features are absent at “non-
46 volcanic” rifted margins, and the presence at some of these margins of exhumed
47 serpentinitized mantle, well-documented by both geophysical studies and by direct
48 sampling in the southern Iberia Abyssal Plain (e.g., [10],[11]), shows that melting can
49 be suppressed by different syn-rift conditions.

50 In both types of rifted continental margin, there are difficulties in measuring
51 accurately the volume of magmatic products using seismic reflection techniques
52 alone. This is due to the high impedance contrast between magmatic intrusions and
53 the surrounding lower continental crustal material, as well as limited spatial
54 resolution, which makes it difficult to image small and discontinuous bodies of

55 intruded material. However, it is possible to put constraints on the total intrusive
56 volume from the average lower-crustal velocity if the end member velocities of the
57 pre-existing crust and the intrusive rocks are known [9]. More importantly, the
58 volume of magmatic products is not constrained uniquely by the tectonic process
59 alone; rather it is also subject to variations in mantle temperature, composition and
60 strain rate.

61 An alternative approach to determining the rifting conditions (encompassing tectonic
62 geometry, strain rate, mantle temperature and composition) is to use the composition
63 of the volcanic products and, where available, upper mantle residues. [12] showed,
64 through modelling, how the rare earth element compositions of syn-rift volcanics on
65 the Labrador margin of eastern Canada and the North Sea Rift are sensitive to mantle
66 temperature, the degree of stretching and the duration of rifting. Using a similar
67 principle, we have developed an integrated kinematic and geochemical model to
68 determine the geochemical compositions of syn-rift melts and their residual mantle
69 source rocks under a variety of rifting conditions. From this model, we demonstrate
70 that the major, minor and rare-earth element geochemistry of the syn-rift melts and
71 their mantle residues are sensitive independently to the extension history and mantle
72 temperature. By inverting the approach, we compare the compositions of syn-rift
73 volcanic products from around the North Atlantic margin with those predicted by our
74 model and hence to infer the most probable rifting conditions prevalent during their
75 genesis.

76 **2. Rifted Margin Melting Model**

77 Various tectonic models for lithospheric stretching at continental margins have been
78 proposed including pure shear models [13], simple shear models [14], and models

79 involving depth-dependent stretching in different forms (e.g., [15]). The simplest
80 models to account for the main features of most rifted margins assume pure shear at a
81 uniform and finite rate. We employ one of these variants, the one-dimensional
82 lithospheric stretching model of [1], which determines several key parameters during
83 rifting: the temperature distribution throughout the lithosphere and asthenosphere and
84 the quantity of melt generated at each increment of rifting and melting.

85 To determine the temperature distribution during rifting, we solve the advection-
86 diffusion equation [16]:

$$87 \quad \frac{\partial T}{\partial t} = \kappa \frac{\partial^2 T}{\partial z^2} - v \left(\frac{\partial T}{\partial z} + h \right),$$

88 where T is temperature, κ is the thermal diffusivity of the mantle, z is the vertical
89 coordinate, v is the vertical velocity of the mantle, and h is the adiabatic temperature
90 gradient. The temperature is corrected for the loss of latent heat of fusion using a
91 method similar to that of [17], assuming a value for the entropy of fusion of 400 J kg^{-1}
92 K^{-1} , and invoking mantle melting under dry solidus conditions. The advection of heat
93 with the melt and the latent heat released by solidification of the melt are ignored
94 since this heat is released in the crust, not in the mantle source region, and its effect on
95 melt generation is negligible [1]. Our model is constructed from a series of depth
96 regions, or cells, the thicknesses of which decrease as a function of rifting progress.
97 Throughout rifting, we assume a constant strain rate, parameterised by the rift
98 duration and the final degree of extension (β_{max}). We use a lithosphere with initial
99 thickness of 125 km that is in thermal equilibrium with the asthenosphere at the start
100 of rifting [18],[19]. Asthenospheric temperature is assumed to be invariant during
101 rifting. Other model parameters are as in Table 1 of [1].

102 The approach of [1] provides an ideal basis for modelling the melt product
103 geochemistry: first, it allows us to test all the rifting parameters of interest while
104 keeping the model simple; second, the melt chemistry parameterisations require
105 calculations of the degree of mantle depletion, temperature and pressure, all of which
106 are tracked through time; third, the composition of the melt and the residue can be
107 determined independently for each depth interval and at each time step in the model.
108 To calculate compositions we assume fractional melting, where the liquid phase
109 separates from the solid residue immediately after it has formed, followed by
110 extraction and lithospheric pooling without further reaction, equilibration or
111 refertilisation of the surrounding mantle matrix. While this assumption is probably a
112 simplification, recent studies of mantle melting and melt extraction based on ^{238}U –
113 ^{230}Th disequilibria find that incremental batch melting and rapid melt extraction is a
114 good approximation of the actual melting process in sub-oceanic mantle [20].
115 Similarly U–Th–Pa–Ra studies of oceanic basalts [21] find results that are consistent
116 with rapid melt migration and extraction via high-porosity channels, with minimal
117 melt-matrix interaction, as a general means of melt extraction from the upper mantle.
118 In addition, the parameterisations we use here enable sequential integrated melting
119 across phase boundaries in the mantle, accommodating melting in both the garnet and
120 spinel lherzolite fields (e.g. [22]). These simplifications allow us to implement several
121 melting schemes and parameterisations in our kinematic and thermal model for
122 comparison.

123 **3. Major Element Composition**

124 Three different major element parameterisations have been implemented [17], [23],
125 [24]. The first two use similar methods to determine melt composition from

126 experimentally derived partition coefficients. In contrast, [17] use empirical fits to
127 data from laboratory melting experiments to derive functions, thus describing
128 effective bulk partition coefficients of each element and the source mantle mineralogy
129 as melting proceeds.

130 **3.1 Source Composition**

131 Before considering the compositions of the magmatic product predicted by our
132 modelling, it is important to note that the composition of syn-rift melts are particularly
133 dependent on the composition of the upper-mantle source. In our modelling, we use a
134 selection of upper-mantle sources, chosen from a variety of studies of tholeiite
135 sources, to both assess the effects of source composition on our results and to inform
136 our choice of a source that yields melts that most closely resemble syn-rift volcanic
137 products.

138 In their modelling, [17] use a ‘Depleted Mantle’ source (DM) made by removing 40%
139 of the mass of a primitive mantle composition [25] by the production of average
140 continental crust (after [26]). [23] use three different sources: (i) ‘Hawaiian Pyrolite’
141 is a synthetic, enriched and fertile spinel lherzolite used in experimental studies of the
142 genesis of Hawaiian tholeiite (after [27]), that is consequently more fertile (i.e., cpx-
143 rich) than ‘DM’; (ii) ‘Tinaquillo lherzolite’ [28], a naturally occurring depleted or
144 refractory spinel lherzolite that is generally more depleted in incompatible elements
145 (except Al and Ca) than DM. ‘Tinaquillo lherzolite’ can be produced by invoking
146 ~5% more melting of a primitive mantle composition than that which has been
147 invoked to produce ‘DM’; and (iii) MORB pyrolite 90, a synthetic MORB source
148 calculated by adding 24% of a mixture comprising 83% N-MORB and 17% primitive
149 olivine, to 76% harzburgite [29]. The [24] source is a naturally occurring depleted

150 abyssal peridotite that is close to the MORB pyrolite 90 composition. Unlike the other
 151 sources mentioned here, it is a real rock, recovered from oceanic fracture zones and as
 152 such, it is attractive since it represents a relatively fertile upper-mantle composition.

153 **3.2 Niu and Batiza [23] and Niu [24] major element parameterisation**

154 The composition of the accumulated melt fraction (C^L) is defined by [23] as the
 155 integral:

$$156 \quad C^L = \frac{1}{X} \int_0^X \frac{C^R}{D + X(1-D)} dX,$$

157 where X is the total melt fraction, C^R is the initial composition of the residue or
 158 ‘solid’ fraction, and D is the partition coefficient. This integral is evaluated at each
 159 time step (i) using:

$$160 \quad C_i^L = \frac{X_{i-1} C_{i-1}^L + X_i - X_{i-1} C_i^{batch}}{X_i},$$

161 where the composition of the incremental batch melt (C_i^{batch}) is calculated from the
 162 residue composition at the end of the previous time step using:

$$163 \quad C_i^{batch} = \frac{C_{i-1}^R}{D + (X_i - X_{i-1})(1-D)}.$$

164 It follows that, for the first increment of melting, $C^L = C^{batch}$ and the residue
 165 composition C_{i-1}^R is that of the source rock. The residue composition is recalculated at
 166 end of each time step from the source rock composition (C_0^R) using:

$$167 \quad C_i^R = \frac{C_0^R - X_i C_i^L}{1 - X_i}.$$

168 Partition coefficients are determined as a function of melt fraction and, with the
169 exception of TiO_2 , of pressure (P). [23] determine the partition coefficient of each
170 major element completely independently using:

$$171 \quad D = e + fX + \frac{g}{X} + hP + i\frac{P}{X}.$$

172 The constants e , f , g , h , and i depend on the source composition.

173 The parameterisation of [24] takes the same form as that of [23] for all partition
174 coefficients with the exception of D_{FeO} . Niu (1997) relates D_{FeO} to D_{MgO} using the
175 following equation:

$$176 \quad D_{\text{FeO}} = 0.317 + 0.0037X - 0.00346P + 0.213D_{\text{MgO}}.$$

177 For low accumulated melt fractions (<10%) the melt compositions determined by
178 both [23] and [24] are incorrect for some elements. The problem is particularly
179 obvious for the Hawaiian pyrolite and Tinaquillo lherzolite source compositions. For
180 these source compositions, as the melt fraction tends toward zero the partition
181 coefficient for FeO falls to zero and for CaO tends toward very high values. This
182 results in a high degree of instability in the models, with instabilities propagating
183 through the calculated compositions of melt and residue from one increment of
184 melting to the next. To reduce this problem, [23] provide an alternative set of partition
185 coefficients for CaO and FeO which give stable results for the Hawaiian pyrolite and
186 Tinaquillo lherzolite sources down to accumulated melt fractions of 5%. We use these
187 alternative partition coefficients to calculate the melt and source residue compositions
188 for accumulated melt fractions down to 5%. For each increment of melting up to an
189 accumulated melt fraction of 5%, we assume that the partition coefficients are fixed.

190 In this way, as the accumulated melt fraction passes 5%, both the melt and residue
 191 compositions match those that would have been formed if the first melt increment had
 192 been at 5%. The partition coefficients for the source compositions ‘MORB pyrolite
 193 90’ [23],[24] appear to yield a stable set of compositional solutions, even at very low
 194 accumulated melt fractions (<1%). For these source compositions we follow the same
 195 procedure as above but fix the minimum partition coefficient to that calculated for an
 196 accumulated melt fraction of 1%.

197 **3.3 Watson and McKenzie [17] major element parameterisation**

198 [17] determine major element melt composition as a function of pressure and melt
 199 fraction using the method of [30] but with modified parameters. Their
 200 parameterisation gives instantaneous melt composition at each stage of melting but,
 201 while it accounts for the mineralogical depletion of the source, the residue
 202 composition is not explicitly defined and we do not calculate it. The instantaneous
 203 melt composition (c) was initially parameterised following [30]:

$$204 \quad c = a + b(1 - X)^{(1-D)/D}.$$

205 To improve the fit to the data, however, [17] sub-divided the melting range into three
 206 phase regions (plagioclase-, spinel- and garnet-lherzolite respectively), $0 < X < X_1$,
 207 $X_1 < X < X_2$ and $X_2 < X < 1$, and provide separate functions for each. They relate
 208 the composition of the accumulated melt fraction to the instantaneous melt
 209 composition using:

$$210 \quad c = \frac{d}{dX}(XC^L),$$

211 then C^L is given by:

212 $C^L = a + \frac{bD}{X} [1 - (1 - X)^{1/D}] + \frac{d}{X}.$

213 **4. Rare Earth Element Composition**

214 The REE composition is determined using the parameterisation of [25]. [25] depleted
215 earth source composition is given in Table 2. The composition of the melt and residue
216 is determined using the same equations as for the major elements in [23] and [24].
217 The partition coefficients are dependent on the plagioclase, spinel and garnet stability
218 fields. [25] provide the proportion of each mineral present in each stability field, and
219 the partition coefficient for each REE within each mineral. For each REE the partition
220 coefficient for the whole mineral assemblage is the sum of each mineral's partition
221 coefficient multiplied by the proportion of that mineral. The stability fields are
222 defined as 25 km and 35 km for spinel-in and plagioclase-out respectively; values that
223 [25] consider reasonable estimates based on the experimental results of [31]. Garnet-
224 in and spinel-out limits are defined by pressure as a function of temperature; the
225 spinel-out boundary is given by:

226 $P = \frac{T + 400}{666.7},$

227 and the garnet-in boundary is given by:

228 $P = \frac{T + 533}{666.7}.$

229 The transition between regimes is assumed to be linear.

230 **5. Model Results**

231 We have run our model for a range of mantle potential temperatures (1200-1500°C) to
232 a stretching factor $\beta_{max} = 50$, which is found to simulate infinite stretching and hence
233 steady-state melt production at a mid-ocean ridge. To explore the effect of strain rate
234 on melt volume and composition, we have, for each temperature step, run the model
235 for a range of rift durations of 1-50 m.y. Results for long rift durations describe
236 behaviour at low strain rates, while results for short durations describe behaviour at
237 high strain rates.

238 **5.1 Melt volume, melt fraction and rifting history**

239 As rifting rates slow, an increasingly significant amount of heat is lost from the upper
240 mantle by conduction through the lithosphere. This heat loss suppresses shallow
241 mantle melting, resulting in a reduced melt fraction and a lower total melt volume or
242 thickness (Fig. 1). Because the base of the melting region is insensitive to rift
243 duration, as rifting rates decrease, the mantle continues to provide melts during rifting,
244 weighting the total aggregated melt composition towards deeper melts and hence
245 effectively increasing the mean pressure of melting (Fig. 2a). A similar result is also
246 seen with lower β_{max} (i.e., with decreasing strain). Aggregated melt compositions
247 approach steady state only after stretching by a factor of $\beta_{max} \geq 5$ (Fig. 2b). With
248 higher mantle temperatures the base of the melting zone moves deeper [30] while the
249 shallowest depths of melting remain unaffected, weighting the aggregated melt
250 composition towards higher mean pressures. The dependence of melting on rifting
251 rate, however, is the same regardless of mantle temperature. Long duration rifting
252 suppresses shallow mantle melting, causing an increase in the mean pressure of
253 melting, a reduction in the mean melt fraction and a lower melt volume or thickness.

254 As a result, the mean melt fraction, total melt volume and mean pressure of melting
255 are critically dependent on both the rifting rate and the initial mantle temperature (Fig.
256 2c,d).

257 Variations in the extent and depth of mantle melting underlie the changes in melt
258 composition (discussed below). Thus it also follows that the composition of syn-rift
259 melts are themselves indicators of the rifting conditions under which they were
260 generated. In the following sections we explore the compositional effects predicted by
261 our modelling and compare actual syn-rift magmatic products to those results in an
262 attempt to distinguish between various rifting conditions.

263 **5.2 Major element trends with varying temperature and rift duration**

264 Despite the effects of using different mantle source compositions, all the
265 parameterisations used in our model yield similar chemical trends for the composition
266 of melts produced under varying mantle temperature and rift duration conditions
267 (Figs. 3, A1-A4). In general, those elements showing decreasing concentrations with
268 increasing mantle temperature (Na, Ti, K, Al and Ca), also show decreasing
269 concentrations with decreasing rift duration (i.e., increasing strain rate). This result
270 reflects changes in the mean melt fraction and subsequent melt volume (Fig. 2c,d) and
271 is to be expected for elements that are generally incompatible in bulk mantle
272 compositions (i.e., such that their concentration in the melt decreases as the extent of
273 melting increases).

274 Two elements (Si and Fe), however, do not show this simple relationship. For the
275 model results using the parameterisations of [23] (Figs. A1-A3) and [24] (Fig. A4), Si
276 decreases in concentration with both increasing mantle temperature and rift duration
277 (i.e., as strain rate decreases). Fe shows an opposite effect, increasing with hotter

278 mantle temperature and longer rift duration (i.e., as strain rate decreases). For the
279 model results using the parameterisation of [17], Si concentrations generally decrease
280 with increasing mantle temperature and rift duration while Fe increases with mantle
281 temperature but is unaffected by rift duration (Fig. 3). The behaviour of Si and Fe is
282 governed by the competing effects of mean melt fraction and mean pressure of
283 melting. Both Si and Fe are particularly sensitive to pressure of melting [32], [33],
284 such that the bulk partition coefficient of silica increases at higher pressures (i.e.,
285 silica becomes more compatible at greater depth), while that for iron decreases. The
286 net result is that while rift duration increases, the mean melt fraction decreases and the
287 mean pressure of melting increases, resulting in lower silica and higher iron
288 concentrations.

289 Our model results show that, as a result of the differing degrees of sensitivity of the
290 major elements to mean melt fraction and mean pressures of melting, any point within
291 mantle-temperature versus rift-duration space yields a unique melt composition.

292 While these unique melt compositions vary depending on the parameterisations and
293 source compositions used in the model, their uniqueness means that the compositions
294 of real rocks may be used as a proxy for mantle temperature and strain rates during
295 continental rifting. While our model is designed to predict the composition of melts
296 generated during continental rifting, it should also predict the composition of N-
297 MORB if rifting is effectively instantaneous and the mantle temperature lies close to
298 that believed to be applicable to the mid-ocean ridge region.

299 **5.3 Residue compositions**

300 The parameterisation of [23] allows the major element composition of the source
301 residue to be continuously recalculated and tracked as melting progresses. The final

302 composition of the residual mantle (Fig. 4) is that which has undergone the most
303 extensive melting by the end of the rifting period. Similar to the compositions of the
304 melt products, the composition of the mantle residue is affected by the pressure and
305 temperature history of melting, as well as by its starting composition. In general,
306 higher mantle temperatures and shorter rift durations result in greater concentrations
307 of elements compatible in the mantle (e.g., magnesium and iron) and decreasing
308 concentrations of incompatible elements (silica, potassium, sodium aluminium,
309 titanium and calcium). While the predicted mantle residue compositions allow the
310 potential for comparison with actual rocks, abyssal peridotites are rarely recovered
311 without significant serpentinisation, which significantly affects the whole rock
312 composition by metasomatic exchange between the rock and seawater.

313 **5.4 REE compositions**

314 Incorporating the partition coefficients for the rare earth elements (REE) and the
315 parameterisation of [25] in our model allows for a calculation of the REE
316 concentrations in the aggregated melt products (Fig. 5). The REE show a general
317 increase in partition coefficient in mafic liquids with decreasing atomic mass –
318 although the bulk partition coefficients between whole rock and melt, in mantle
319 mineralogy, remain substantially less than one. Hence the behaviour of the REE, with
320 varying mantle temperature and rift duration, are similar to that of the incompatible
321 major elements (e.g., sodium, potassium and titanium). As the mantle temperature
322 increases and the rift duration decreases, the concentrations of the REE decrease
323 rapidly. An exception to this behaviour is hafnium, which decreases in concentration
324 sharply between low and moderate mantle temperatures and at short rift durations, but
325 changes little at higher temperatures and at longer rift durations. The reason for this is
326 the pressure dependant behaviour of hafnium such that is compatible in garnet [34].

327 At high mantle temperatures and slow rifting, the mean pressure of melting is high.
328 This effect weights the aggregated melt composition towards those increments drawn
329 from the garnet-lherzolite stability field where hafnium is retained in the residual
330 garnet.

331 **6. Comparison with actual rocks**

332 In the following section, we compare the results of our model against actual volcanic
333 products recovered from rifted margins. Like most mantle melting models, our model
334 predicts the composition of primary melts, generated under a variety of conditions.
335 These melts undergo variable degrees of fractional crystallisation before being
336 erupted [35], [36], the effects of which are to increase the concentrations of
337 incompatible elements and reduce the concentrations of compatible elements. The
338 potential consequences of these effects, when comparing actual volcanic products
339 with our model results, are to overestimate the rift duration and underestimate the
340 mantle temperature. In order to minimize these effects we have chosen to compare
341 only the most primitive rocks (i.e. those from a narrow range of high MgO
342 concentrations), allowing us to discriminate between different rifting durations and
343 initial mantle temperatures.

344 The results of these comparisons are shown in two ways: as a multi-element spider
345 diagram (where calculated elemental concentrations are normalized to a known
346 reference material, such as N-MORB), and as misfit diagrams (which express the
347 extent of misfit between a particular whole rock composition and a range of
348 compositions, each calculated for specific mantle temperatures and rift durations).

349 The misfit (f_m) for each unique combination of mantle temperature and rift duration
350 is calculated from the following equation:

$$351 \quad f_m = \frac{I}{N} \sum_{i=1}^N \frac{(E_{ip} - E_{io})^2}{(\delta_{min}^{max} E_{ip})^2}$$

352 where E_{ip} is the predicted concentration for the i^{th} major element, at a unique mantle
353 temperature and rift duration; E_{io} is the observed concentration for that element in the
354 reference rock; $\delta_{min}^{max} E_{ip}$ is the range of predicted concentrations for that element; and
355 N is the number of elements.

356 Hence the final misfit value for a particular rock is the average of the root-mean-
357 squares (rms) of the misfits of all the elements to the entire range of model results.
358 Each element's misfit is normalised to the range of that element's concentration as
359 predicted by the model, so that all elements, regardless of their percentage of the total
360 rock, are given equal weighting in the misfit. It should be noted that some element
361 concentrations are more accurately and precisely measured than others. Also, the
362 behaviour of some elements during melting is better known, while other elements are
363 more or less susceptible to secondary alteration. However, weighting one element
364 more than another cannot be justified without knowing the history of each element
365 during the melting, fractional crystallisation and alteration stages of a particular rock.
366 The only exception that we make is for potassium. Potassium is not included in the
367 misfit functions because its concentration is poorly known in the depleted upper
368 mantle (see below) – it is often associated with metasomatic mantle enrichment and it
369 is especially strongly affected by secondary alteration.

370 **6.1 Comparison with N-MORB**

371 As an initial assessment of our model, we compare normal mid-ocean ridge basalt (N-
372 MORB, [37]) to the predicted compositions of primary melts using various
373 parameterisations, mantle sources, mantle potential temperatures (1300°C and
374 1500°C) and rift durations of 1 and 50 m.y. The resultant liquids, normalized to N-
375 MORB, show the effects of increasing rift duration and mantle temperature (Fig. 6).
376 These effects are especially apparent for the incompatible elements (K, Ti, Na and Ca)
377 which increase in concentration for lower melt fractions and longer rift durations, and
378 which mimic the effects of more fertile mantle sources (e.g., Hawaiian pyrolite).

379 Of the five parameterisations and source compositions used in our model, the results
380 obtained by using the parameterisation of [17], at 1300°C and a rift duration of 1 m.y.,
381 produce a composition that most closely resembles N-MORB. Figure 7 shows results
382 for the REE concentrations, normalised to N-MORB [37], predicted for temperatures
383 of 1300°C and 1500°C and rift durations of 1 m.y. and 50 m.y. The resulting
384 predicted liquid produced at a mantle temperature of 1300°C and almost
385 instantaneous rifting (1 m.y.) compares favourably with N-MORB while those melts
386 produced at higher temperatures are more depleted, and that generated at 1300°C and
387 50 m.y. is more enriched.

388 Despite the close fit between the predicted major elemental concentrations and the
389 composition of N-MORB, potassium remains poorly reproduced. This problem exists
390 for all five parameterisations and sources and probably results from either incorrect
391 assumptions for the concentration of potassium in the source, poorly constrained
392 partition coefficients, or anomalously low potassium concentrations in our

393 normalising N-MORB composition. This observation reinforces our decision not to
394 use potassium concentrations in our misfit function.

395 Figures 8a and b shows the minimum misfit between primitive N-MORB [37] and the
396 model results incorporating the parameterizations of [17] and [24] using the MPY90
397 source. The misfit values are minimised at a temperature and rift duration that yields a
398 liquid that lies closest in composition to primitive N-MORB. Of these results, the
399 misfit generated by the model incorporating the parameterization of [17] is minimised
400 at a mantle potential temperature of 1260°C and a rift duration of 2 m.y. This is close
401 to the mantle potential temperature of 1280°C, used by [17] in their original
402 parameterization to model parental N-MORB genesis at a mid-ocean ridge. In
403 comparison, the other parameterizations used in our model generally yield poorer
404 misfits with minima at higher mantle temperatures and/or longer rifting duration (i.e.,
405 slower rifting rates). For example, using the parameterization of [24] yields higher
406 mantle temperatures and longer rift durations, respectively, of: 1430°C and 14 m.y.
407 for the MORB pyrolite source MPY90; 1406°C and 1 m.y. for the Hawaiian pyrolite
408 source; and 1420°C and 8 m.y. for the Tinaquillo lherzolite source.

409 **6.2 Comparison with North Atlantic Margin Volcanic products**

410 In the following section, we calculate the misfit functions for a number of volcanic
411 suites from around the northwest Atlantic margin, formed during the initial opening of
412 the North Atlantic. Several volcanic sequences have been collected at each site by
413 DSDP and ODP drilling expeditions. In comparing these rocks with our model, we
414 have chosen an average of the most primitive (i.e., highest MgO - at least 7 wt.%),
415 least phyric, and least altered rocks (e.g., having the lowest reported 'loss on ignition'
416 values) of basaltic composition from each sequence. The geotectonic setting of these

417 break-up lavas varies considerably: from the volcanic rifted margin of East Greenland
418 at 63°N (ODP Sites 915, 917, 918, 989, 990) and its conjugate at Edoras Bank margin
419 (DSDP Site 553 and 554), to the ‘non-volcanic’ margin of Goban Spur (DSDP Sites
420 550 and 551). These rifts were initiated at varying distance and time from the mantle
421 melting anomaly (Icelandic plume) that was later to form Iceland. Hence we might
422 predict a variation in mantle temperature during rifting with relatively higher mantle
423 temperatures closer to the centre of the melting anomaly and lower temperatures both
424 further away and prior to the start of the anomaly [38].

425 We have chosen to calculate the major element misfits to our model using the
426 parameterization of [17], since this method gives the best fit to N-MORB.
427 Furthermore, for the remaining parameterizations other than [17], most of the syn-rift
428 volcanic suites plot out of the range of the predicted mantle temperature and rift
429 duration. Because we have not corrected for AFC processes, the minimum misfits
430 predict relative mantle temperatures and rifting rates rather than absolute conditions
431 during rifting. Not all of the whole rock analyses available for comparison to our
432 model include a full set of REE concentrations, so we have decided to omit the REEs
433 from any of the misfit functions. Figure 5 shows that the REEs are more sensitive to
434 mantle temperature than rift duration. However, since rift duration is the main
435 parameter affecting mean pressure of melting, we would recommend including the
436 concentration of heavy REEs (e.g., Lu and Hf) as well as the light REEs (e.g., La and
437 Sm) in any future misfit functions.

438 **6.2.1 East Greenland margin**

439 ODP Legs 152 and 163 drilled a transect across the East Greenland volcanic margin at
440 63°N, where drilling penetrated a thick succession of seaward dipping reflector

441 sequence (SDRS) volcanic rocks that erupted during break-up of the North Atlantic in
442 the early Tertiary. The western-most holes are well within the influence of the proto-
443 Iceland plume [38], while the easternmost holes are on thickened oceanic basement.
444 With both a decrease in age and increase in distance east, the SDRS lava succession is
445 thought to represent a transition from continental break-up to seafloor spreading [9],
446 [39], [40]. On the basis of their position and age, the lava sequences recovered in the
447 holes can be ordered according the progression from continental rifting to initial
448 seafloor spreading: 917A Lower lavas are the oldest and were erupted during
449 continental rift initiation with Site 917A Upper and Site 989 lavas being later syn-rift
450 eruptions on stretched continental crust. Site 918D lavas were erupted at the transition
451 from the late continental rifting to early oceanic spreading. Holes 990A and 915A are
452 both located close together and recovered SDRS lavas forming the youngest
453 extrusives prior to the onset of full seafloor spreading.

454 Recent seismic models ([8], [41]) suggest a crustal thickness along the drilling
455 transect of up to 18 km [41] at the time of break-up, reducing to 8-10 km thickness 6-
456 12 m.y. after break-up [8]. [8] attribute the initial melt thickness to a transient elevated
457 temperature anomaly of $\sim 1400 \pm 50^\circ\text{C}$ in the asthenosphere; while transient active
458 asthenospheric upwelling could produce the same melt thickness pattern, the location
459 is thought to be sufficiently distal to the Iceland hotspot that this process is not a
460 significant factor.

461 The parameters in our melting model do not incorporate the effect of a transient
462 temperature anomaly. Such a transient could be achieved by adding a high
463 temperature layer directly beneath the continental lithosphere [41], which travels
464 upward, and passes through the melting region, as rifting proceeds. [42] show that a

465 1425-1525°C, 50 km thick layer can produce a similar melt thickness pattern to the
466 seismic observations [8]. In such models, the majority of the melt, especially that
467 located near to the ODP Sites where initial break-up occurred, is formed at the
468 elevated asthenospheric temperature. In this case, our melting model calculates the
469 average melt chemistry formed during the entire rift period, and is therefore biased
470 toward the chemical signature of the high temperature melt.

471 Figure 8c shows the misfit functions for the East Greenland margin early syn-rift
472 SDRS lavas (Sites 917L and 917U, 989) while Figure 8d shows data from the SDRS
473 for the later and/or more oceanward syn-rift sequence. In each case the mantle
474 temperature prediction is more constrained than the rifting rate, with both groups of
475 SDRS lavas predicted to have formed under similar conditions: slow rifting rates (i.e.,
476 rift duration of ~40 m.y.) and with mantle temperatures of ~1400°C. The elevated
477 mantle temperatures are consistent with the presence of a thermal anomaly associated
478 with the Icelandic mantle plume [2], [9], [38], [43]. An excess temperature of ~140°C
479 for the syn-rift mantle beneath East Greenland, compared with asthenosphere yielding
480 N-MORB, is also compatible with the enhanced thickness of SDRS lavas and the high
481 seismic velocities and thicknesses of the magmatic lower-crustal intrusion that is
482 characteristic of this margin [5], [9], [40]. As seafloor spreading progressed, the
483 mantle temperature decreased by ~70–80°C over the first 10 Ma following continental
484 breakup [40]. This decrease might be a result of exhaustion of a finite hot layer of
485 mantle [42], a reduction in the diameter of the plume head (as proposed by [38]), drift
486 of the plume stem away from the region, a secular decline in the plume mantle
487 temperature, or a combination of all of these effects [4].

488 **6.2.2 Edoras Bank margin**

489 DSDP Leg 81 drilled three sites across the Edoras Bank on the western Atlantic
490 margin at 56°N. Drilling at the sites penetrated SDRS lavas of late Paleocene/early
491 Eocene [44]. Figure 8e shows the average misfit functions for the Edoras Bank
492 margin basalts from holes 553 and 554. Sites 552, 553 and 554 are located
493 progressively westward (i.e., oceanward) across the rifted margin. Sites 553 and 554
494 recovered basalt that is sufficiently fresh to be used in our modelling, but Site 552
495 lavas are too strongly altered and contaminated by continental crust to be included in
496 our analysis. Site 553 is situated on stretched continental crust while Site 554 is on the
497 outer high between seaward dipping reflectors [4], [44], [45].

498 The average misfit functions of the remaining rocks constrain better the mantle
499 temperature than the rifting rate. The Edoras Bank margin appears to have started
500 rifting with a mantle that was between 1350 and 1375°C (i.e., 25-50°C cooler than the
501 ODP transect off East Greenland). This slightly lower mantle temperature is
502 consistent with the Edoras Bank margin being located (at 56°N) further to the south of
503 the East Greenland sites at 63°N, and hence at a greater distance from the centre of
504 the Icelandic mantle plume. It is also consistent with slightly thinner SDRS and the
505 thickness of lower-crustal magmatic intrusions at the Edoras Bank margin (at 56°N),
506 compared with the East Greenland margin at 63°N [4]. The subsidence calculations in
507 [4] show a somewhat higher mantle temperature than our estimates from the
508 geochemistry, but the overall trends are equivalent, i.e., the temperature decreases
509 away from the plume centre. We also note that the subsidence calculations assume a
510 single phase of passive upwelling. If there were a component of active upwelling in
511 the mantle beneath the initial rift at the time of continental break-up, as indeed may be
512 the case [41], rather lower temperatures would be required to give the same

513 subsidence. If this were the case then the subsidence and geochemical mantle
514 temperature constraints could be very similar.

515 **6.2.3 Goban Spur margin**

516 DSDP Leg 80 drilled several sites on the western Atlantic margin at 49°N. Unlike the
517 East Greenland and Edoras Bank margins, which are considered to have been
518 influenced by elevated mantle temperatures, the Goban Spur margin does not have a
519 significant high velocity lower-crustal section and is considered have had little syn-rift
520 magmatism [46]. Drilling recovered basalts at two sites, 550 and 551, both on the
521 ocean-continent transition. At these locations, the structure of the Goban Spur margin
522 is complex, with an east-west oriented offset forming a ridge that separates Site 551
523 (to the northeast) from Site 550 (to the southwest). Wide-angle seismic data indicate
524 that Site 551 is underlain by highly thinned continental crust [47]. There are no wide-
525 angle seismic constraints for Site 550, though this site lies about 50 km along-strike
526 from a region where the basement is interpreted as serpentinised mantle [47]. If this
527 basement is exhumed continental mantle, as inferred on the west Iberia margin [11], it
528 is then unclear which site hosts lavas formed later in the rifting process. Using lavas
529 from both sites 550 and 551 to predict the rifting conditions for this margin, Figure 8f
530 shows the average misfit functions that have a minimum for a mantle temperature of
531 1260-1285°C and a rift duration of 8-13 m.y. The inferred rift durations from melt
532 compositions are close to the estimated duration of 14-22 m.y. based on stratigraphic
533 evidence [47], while melting temperatures are close to those for N-MORB genesis.
534 Our modelling suggests that syn-rift mantle temperatures for Goban Spur were ~80°C
535 cooler than the East Greenland margin at 63°N, and 60°C cooler than the Edoras Bank
536 margin. This result is not especially surprising, since the mid- to late Cretaceous age

537 of rifting at Goban Spur was prior to the known initiation of the Icelandic mantle
538 plume [43].

539 **7. Summary and conclusions**

540 We have developed a numerical model that integrates kinematic and geochemical
541 parameters during continental stretching and rifting to allow us to predict the
542 composition of magmatic products generated under a range of continental rifting
543 conditions. Using a modular scheme, we have integrated the lithospheric stretching
544 model of [1], with three different major element parameterisations: [17], [23] and
545 [24]. We also incorporate a parameterisation for the rare earth elements based on [25].
546 Our model shows how the geochemistry of basalts erupted during rifting can be used
547 to infer relative differences in mantle temperature and rift duration. These predictions
548 can, in turn, be used to predict the volume of syn-rift magmatism, as expressed both
549 by extrusive lavas that form SDRS packages and intrusion of the stretched continental
550 lithosphere, and hence the thermal evolution and uplift/subsidence histories for rifted
551 continental margins. Comparison of our model results, using a range of
552 parameterisations, with actual mid-ocean ridge basalts (i.e., instantaneous rifting)
553 reveals close reproduction of N-MORB compositions when using the parameterisation
554 of [17]. Calculated misfit functions between predicted compositions and actual
555 volcanic rocks from around the North Atlantic margin (Fig. 8c-f) confirm that syn-rift
556 lavas erupted closer to the centre of the Icelandic hotspot were derived from hotter
557 average mantle temperatures than those erupted further away. The composition of
558 rocks erupted within the influence of the Iceland mantle plume indicate higher mantle
559 temperatures than those erupted on non-volcanic margins away from the influence of
560 mantle plumes.

561 Because our model predicts the composition of primitive melts that are in equilibrium
562 with the mantle, we recommend comparing only the freshest and most primitive
563 basaltic rocks with our model results (e.g., ideally high-magnesium glasses).
564 Fractional crystallisation will result in an apparent over estimate of rift duration
565 and/or an underestimate of mantle potential temperature. We also recommend that
566 care be taken to screen samples for evidence of crustal contamination, either through
567 isotopic analysis (Pb and Nd ratios) and/or scrutiny of the high-field strength trace
568 elements that are indicators of crustal contamination (e.g. Zr and Nb). We further
569 suggest that any misfit function utilising REE compositions should weigh equally the
570 light and heavy REE's to maximise sensitivity to both the mean extent and the
571 pressure of melting, which are proxies for mantle temperature and rift duration
572 respectively.

573 **Acknowledgements**

574 This project was funded by the Natural Environment Research Council's Ocean
575 Margins (LINK) programme, grant reference number NER/T/S/2000/00650.

576 **Appendix**

577 Supplementary data associated with this article consists of the major element
578 composition of the melt fraction for varying rift duration and asthenospheric mantle
579 potential temperature for four additional source compositions (Figures A1-A4).

580

581 **References**

- 582 [1] J.W. Bown, R.S. White, The effect of finite extension rate on melt generation at
583 continental rifts, *J. Geophys. Res.* 100 (1995) 18011—18030.
- 584 [2] R. White, D. McKenzie, Magmatism at rift zones: the generation of volcanic
585 continental margins and flood basalts, *J. Geophys. Res.* 94 (1989) 7685—7729.
- 586 [3] C.E. Keen, R.C. Courtney, S.A. Dehler, M.-C. Williamson, Decompression
587 melting at rifted margins: comparison of model predictions with the distribution
588 of igneous rocks on the eastern Canadian margin, *Earth Planet. Sci. Lett.* 121
589 (1994) 403—416.
- 590 [4] A.J. Barton, R.S. White, Crustal structure of the Edoras Bank margin and
591 mantle thermal anomalies beneath the North Atlantic, *J. Geophys. Res.* 102
592 (1997) 3109—3129.
- 593 [5] J. Korenaga, W.S. Holbrook, G.M. Kent, P.B. Kelemen, R.S. Detrick, H.-C.
594 Larsen, J.R. Hopper, T. Dahl-Jensen, Crustal structure of the southeast
595 Greenland margin from joint refraction and reflection seismic tomography, *J.*
596 *Geophys. Res.* 105 (2000) 21591—21614.
- 597 [6] P.B. Kelemen, W.S. Holbrook, Origin of thick, high-velocity igneous crust
598 along the US East-Coast Margin, *J. Geophys. Res.* 100 (1995) 10077—10094.
- 599 [7] N.I. Christensen, W.D. Mooney, Seismic velocity structure and composition of
600 the continental crust: a global view, *J. Geophys. Res.* 100 (1995) 9761—9788.
- 601 [8] W.S. Holbrook, H.-C. Larsen, J. Korenaga, T. Dahl-Jensen, I. Reid, P. B.
602 Kelemen, J.R. Hopper, G.M. Kent, D. Lizzaralde, S. Bernstein, R.S. Detrick,

- 603 Mantle thermal structure and active upwelling during continental breakup in the
604 North Atlantic, *Earth Planet. Sci. Lett.* 190 (2001) 251—266.
- 605 [9] R.S. White, L.K. Smith, A.W. Roberts, P.A.F. Christie, N.J. Kusznir, Lower-
606 crustal intrusion on the North Atlantic continental margin, *Nature* 452 (2008)
607 460—464.
- 608 [10] S.M. Dean, T.A. Minshull, R.B. Whitmarsh, K.E. Louden, Deep structure of the
609 ocean-continent transition in the southern Iberia Abyssal Plain: II. The IAM-9
610 transect at 40°20'N, *J. Geophys. Res.* 105 (1999) 5859—5885.
- 611 [11] R.B. Whitmarsh, G. Manatschal, T.A. Minshull, Evolution of magma-poor
612 continental margins from rifting to seafloor spreading, *Nature* 413, 2001, 150—
613 154.
- 614 [12] M.-C. Williamson, R.C. Courtney, C.E. Keen, S.A. Dehler, The volume and
615 rare earth element concentrations of magmas generated during finite stretching
616 of the lithosphere, *J. Petrol.* 36 (1995) 1433—1453.
- 617 [13] D. McKenzie, Some remarks on the development of sedimentary basins, *Earth*
618 *Planet. Sci. Lett.* 40 (1978) 25—32.
- 619 [14] B. Wernicke, Uniform sense normal simple shear of the continental lithosphere,
620 *Can. J. Earth Sci.* 22 (1985) 108—125.
- 621 [15] M. Davis, N. Kusznir, Depth-dependent lithospheric stretching at rifted
622 continental margins, in: G.D. Karner (Ed.), *Proceedings of NSF Rifted Margins*
623 *Theoretical Institute, Columbia University Press, 2004, pp. 92—136.*
- 624 [16] W.H. Press, B.P. Flannery, S.A. Teukolsky, W.T. Vetterling, *Numerical*
625 *Recipes in FORTRAN 77: The art of scientific computing, Cambridge*
626 *University Press, New York, 1992, 992 pp.*

- 627 [17] S. Watson, D. McKenzie, Melt generation by plumes: a study of Hawaiian
628 volcanism, *J. Petrol.* 32 (1991) 501—537.
- 629 [18] B. Parsons, J.G. Sclater, An analysis of the variation of oceanfloor bathymetry
630 and heat flow with age, *J. Geophys. Res.* 82 (1977) 803—827.
- 631 [19] H.N. Pollack, D.S. Chapman, On the regional variations of heat flow,
632 geotherms, and lithospheric thickness, *Tectonophysics* 38 (1977) 279—296.
- 633 [20] M. Condomines, O. Sigmarsson, U-238–Th-230 disequilibria and mantle
634 melting processes: a discussion, *Chemical Geology* 162 (2000) 95—104.
- 635 [21] A. Stracke, B. Bourdon D. McKenzie, Melt extraction in the Earth's mantle:
636 Constraints from U–Th–Pa–Ra studies in oceanic basalts, *Earth Planet Sci. Lett.*
637 244 (2006) 97—112.
- 638 [22] A. Prinzhofer, C.J. Allègre, Residual peridotites and the mechanisms of partial
639 melting, *Earth Planet Sci. Lett.* 74 (1985) 251—265.
- 640 [23] Y. Niu, R. Batiza, An empirical method for calculating melt compositions
641 produced beneath mid-ocean ridges: application for axis and off-axis
642 (seamounts) melting, *J. Geophys. Res.* 96 (1991) 21753—21777.
- 643 [24] Y. Niu, Mantle melting and melt extraction processes beneath ocean ridges:
644 evidence from abyssal peridotites, *J. Petrol.* 38 (1997) 1047—1074.
- 645 [25] D. McKenzie, R.K. O’Nions, Partial melt distributions from inversion of rare
646 earth element concentrations, *J. Petrol.* 32 (1991) 1021—1091.
- 647 [26] S.R. Taylor, S.M. McLennon, *The Continental Crust: Its Composition and*
648 *Evolution*, Blackwell, Oxford, 1985, 312 pp.

- 649 [27] D.H. Green, Experimental melting studies on a model upper mantle composition
650 at high pressure under water-saturated and water-unsaturated conditions, *Earth*
651 *Planet. Sci. Lett.* 19 (1973) 37—53.
- 652 [28] A.L. Jaques, D.H. Green, Anhydrous partial melting of peridotite at 0-15 kb
653 pressure and the genesis of tholeiitic basalts, *Contrib. Miner. Petrol.* 73 (1980)
654 287—310.
- 655 [29] D.H. Green, W.O. Hibberson, A.L. Jaques, Petrogenesis of mid-ocean ridge
656 basalts, in: M.W. McElhinney (Ed.), *The Earth: Its Origin, Structure and*
657 *Evolution*, Academic Press, London, 1979, pp. 265—299.
- 658 [30] D. McKenzie, M.J. Bickle, The volume and composition of melt generated by
659 extension of the lithosphere, *J. Petrol.* 29 (1988) 625—679.
- 660 [31] D.C. Presnall, J.D. Hoover, High pressure phase equilibrium constraints on the
661 origin of mid-ocean ridge basalts, in: B. Mysen (Ed.), *Magmatic Processes:*
662 *Physicochemical Principles*, *Geochem. Soc. Spec. Pub.* 1, 1987, pp. 75—89.
- 663 [32] E.M. Klein, C.H. Langmuir, Global correlations of ocean ridge basalt chemistry
664 with axial depth and crustal thickness, *J. Geophys. Res.* 92 (1987) 8089—8115.
- 665 [33] C.H. Langmuir, E.M. Klein, T. Plank, Petrological systematics of mid-ocean
666 ridge basalts: Constraints on melt generation beneath ocean ridges, in: J. Phipps
667 Morgan, D.K. Blackman, J.M. Sinton (Eds.), *Mantle Flow and Melt Generation*
668 *at Mid-Ocean Ridges*, *Geophys. Mon.* 71, 1992, pp. 183—280.
- 669 [34] V.J.M. Salters, S.R. Hart, The hafnium paradox and the role of garnet in the
670 source of mid-ocean-ridge basalts, *Nature* 342 (1989) 420—422.
- 671 [35] R.J. Kinzler, T.L. Grove, Primary Magmas of Mid-Ocean Ridge Basalts 2.
672 Applications, *J. Geophys. Res.* 97 (1992) 6907—6926.

- 673 [36] E. Stolper, A phase-diagram for mid-ocean ridge basalts: Preliminary results
674 and implications for petrogenesis, *Contrib. Mineral. Petrol.* 74 (1980) 13—27.
- 675 [37] S.R. Hart, J. Blusztajn, H.J.B. Dick, P.S. Meyer, K. Muehlenbachs, The
676 fingerprint of seawater circulation in a 500-meter section of ocean crust
677 gabbros, *Geochimica et Cosmochimica Acta* 63 (1999) 4059—4080.
- 678 [38] R.S. White, Rift-plume interaction in the North Atlantic, *Phil. Trans. Roy. Soc.*
679 *A.* 355 (1997) 319—339.
- 680 [39] J.G. Fitton, A.D. Saunders, L.M. Larsen, B.S. Hardarson, M.J. Norry, Volcanic
681 rocks from the southeast Greenland margin at 63°N: Composition, petrogenesis,
682 and mantle sources, in: A.D. Saunders, H.C. Larsen, S.W. Wise Jr. (Eds.),
683 *Proceedings of the Ocean Drilling Program, Scientific Results*, vol. 152, Ocean
684 *Drilling Program*, College Station, Tex., 1998, pp. 331—350.
- 685 [40] R.S. White, L.K. Smith, Crustal structure of the Hatton and the conjugate east
686 Greenland rifted volcanic continental margins, NE Atlantic, *J. Geophys. Res.*, in
687 press.
- 688 [41] J.R. Hopper, T.Dahl-Jensen, W.S. Holbrook, H.C.Larsen, D. Lizarralde, J.
689 Korenaga, G.M. Kent, P.B. Kelemen, Structure of the SE Greenland margin
690 from seismic reflection and refraction data: Implications for nascent spreading
691 center subsidence and asymmetric crustal accretion during North Atlantic
692 opening, *J. Geophys. Res.* 108 (2003) doi:10.1029/2002JB001996.
- 693 [42] J.J. Armitage, T.J. Henstock, T.A. Minshull, J.R. Hopper, Modelling the
694 composition of melts formed during continental breakup of the Southeast
695 Greenland margin, *Earth Planet. Sci. Lett.* 269 (2008) 248—258.

- 696 [43] R.S. White, A hot-spot model for early Tertiary volcanism in the N. Atlantic, in:
697 A.C. Morton, L.M. Parson (Eds.), *Early Tertiary Volcanism and the Opening of*
698 *the NE Atlantic*, Geol. Soc. Spec. Pub. 39, 1988, pp. 3—13.
- 699 [44] D.G. Roberts, D. Schnitker, et al., *Initial Reports of the Deep Sea Drilling*
700 *Project*, vol. 81, U.S. Government Printing Office, Washington, 1984, 923 pp.
- 701 [45] J. Brodie, J.G. Fitton, *Data report: Composition of basaltic lavas from the*
702 *seaward-dipping reflector sequence recovered during deep sea drilling project*
703 *leg 81 (Hatton Bank)*, in: A.D. Saunders, H.C. Larsen, S.W. Wise Jr. (Eds.),
704 *Proceedings of the Ocean Drilling Program, Scientific Results*, vol. 152, Ocean
705 *Drilling Program*, College Station, Tex., 1998, pp. 431—435.
- 706 [46] R.C. Maury, H. Bellon, H. Bougault, J.L. Joron, M. Bohn, P.C. de Graciansky,
707 *Oceanic tholeiites from Leg 80 sites (Celtic Sea passive margin, northeastern*
708 *Atlantic): Geochemistry and mineralogy*, in: P.C. de Graciansky, et al., *Initial*
709 *Reports of the Deep Sea Drilling Project*, vol. 80, U.S. Government Printing
710 *Office*, Washington, 1985, pp. 939—946.
- 711 [47] A.D. Bullock, T.A. Minshull, *From continental extension to seafloor spreading:*
712 *crustal structure of the Goban Spur rifted margin, southwest of the UK,*
713 *Geophys. J. Int.* 163 (2005) 527—546.
- 714

715 **Figure Captions**

716 **Figure 1:** (a) Upper panel: contoured plot of temperature (solid lines) versus depth,
717 through time, for the rift model with an asthenospheric mantle temperature of 1300°C,
718 a rift duration of 5 m.y., and $\beta_{\max} = 50$. Equilibrium melt fraction is shaded yellow to
719 red and contoured with dotted lines. Lower panel: accumulated melt thickness through
720 time. (b) As (a) but for a rift duration of 20 m.y.

721 **Figure 2:** (a) Contoured average (mean) depth of melting at the end of the rift period;
722 the model has $\beta_{\max} = 50$, an initial lithospheric thickness of 125 km, and a constant
723 strain rate throughout the rift period; a rift duration of 1 m.y. approximates
724 instantaneous rifting. (b) as (a) but for varying β and asthenospheric mantle
725 temperatures between 1250°C and 1500°C (black lines); the grey line represents the
726 depth at which maximum melting takes place. (c) Contoured melt fraction within the
727 region of melting and (d) melt thickness accumulated at the end of the rift period,
728 using the same model as (a).

729 **Figure 3:** The major element composition of the melt fraction in wt%, for varying rift
730 duration and asthenospheric mantle potential temperature, calculated using the
731 parameterisation of [17]. The model uses the same depleted mantle (DM) source
732 composition (spinel lherzolite) as employed by [30] and has an initial lithospheric
733 thickness of 125 km with a constant strain rate throughout the rift period, and $\beta_{\max} =$
734 50.

735 **Figure 4:** Major element composition of the residue in wt%, for varying rift duration
736 and asthenospheric mantle potential temperature, calculated using the
737 parameterisation of [24]. The model assumes a Hawaiian pyrolite source composition

738 and has an initial lithospheric thickness of 125 km, a constant strain rate throughout
739 the rift period, and $\beta_{\max} = 50$.

740 **Figure 5:** Rare earth element composition (ppm) of the melt fraction for varying rift
741 duration and asthenospheric mantle potential temperature, calculated using the
742 parameterisation of [25]. Model parameters are the same as in Figure 2a.

743 **Figure 6:** Multi-element spider diagram for the major element compositions of
744 aggregated melts, normalised to average North Atlantic N-MORB [37], calculated
745 from the five different parameterisations, for rift durations of 1 m.y. and 50 m.y. and
746 asthenospheric mantle potential temperatures of 1300°C and 1500°C. The plots show
747 that the parameterisations of [17], [23] and [24] (the latter two both using a MORB
748 pyrolite source) that invoke mantle temperatures of 1300°C produces aggregated
749 melts that are closest in major element composition to N-MORB.

750 **Figure 7:** Rare earth element compositions for melt fractions generated at
751 asthenospheric mantle potential temperatures of 1300°C and 1500°C, and rift
752 durations of 1 m.y. and 50 m.y., normalised to North Atlantic N-MORB [37].

753 **Figure 8:** Misfit diagrams between model outputs and measured compositions. (a)
754 The misfit between N-MORB (average northern Mid-Atlantic Ridge [37]) and our
755 model output using the parameterisation of [24] for a MORB pyrolite source, yields a
756 best fit mantle temperature of $\sim 1430^\circ\text{C}$ at 14 m.y. (b) The misfit between N-MORB
757 (average northern Mid-Atlantic Ridge [37]) and our model output using the
758 parameterisation of [17] yields a best fit mantle temperature of 1260°C and a rift
759 duration of 2 m.y. (c) Misfit function for the East Greenland margin early syn-rift
760 SDRS lavas (Sites 917L and 917U, 989). The minimum misfit values indicate where

761 the average of the composition of the lavas best fits the melt composition predicted by
762 our model using the parameterisation of [17]. (d) As (c) for later syn-rift eruptions at
763 sites 918D, 990A and 915A. (e) As (c) for the Edoras Bank margin syn-rift basalts. (f)
764 As (c) for the Goban Spur margin syn-rift basalts. The model indicates that mantle
765 temperatures beneath the Goban Spur margin were close to N-MORB conditions
766 during the Cretaceous rift to drift transition.

767

768 **Appendix**

769 **Figure A1:** The major element composition of the melt fraction in wt%, for varying
770 rift duration and asthenospheric mantle potential temperature, an initial lithospheric
771 thickness of 125 km with a constant strain rate throughout the rift period, and $\beta_{\max} =$
772 50, calculated using the parameterisation of [23] for Hawaiian pyrolite source
773 composition.

774 **Figure A2:** The major element composition of the melt fraction in wt%, for varying
775 rift duration and asthenospheric mantle potential temperature, an initial lithospheric
776 thickness of 125 km with a constant strain rate throughout the rift period, and $\beta_{\max} =$
777 50, calculated using the parameterisation of [23] for Tinaquillo lherzolite source
778 composition.

779 **Figure A3:** The major element composition of the melt fraction in wt%, for varying
780 rift duration and asthenospheric mantle potential temperature, an initial lithospheric
781 thickness of 125 km with a constant strain rate throughout the rift period, and $\beta_{\max} =$
782 50, calculated using the parameterisation of [23] for MORB pyrolite 90 source
783 composition.

784 **Figure A4:** The major element composition of the melt fraction in wt%, for varying
785 rift duration and asthenospheric mantle potential temperature, an initial lithospheric
786 thickness of 125 km with a constant strain rate throughout the rift period, and $\beta_{\max} =$
787 50, calculated using the parameterisation of [24].

788

Figure 1

[Click here to download Figure: fig1.eps](#)

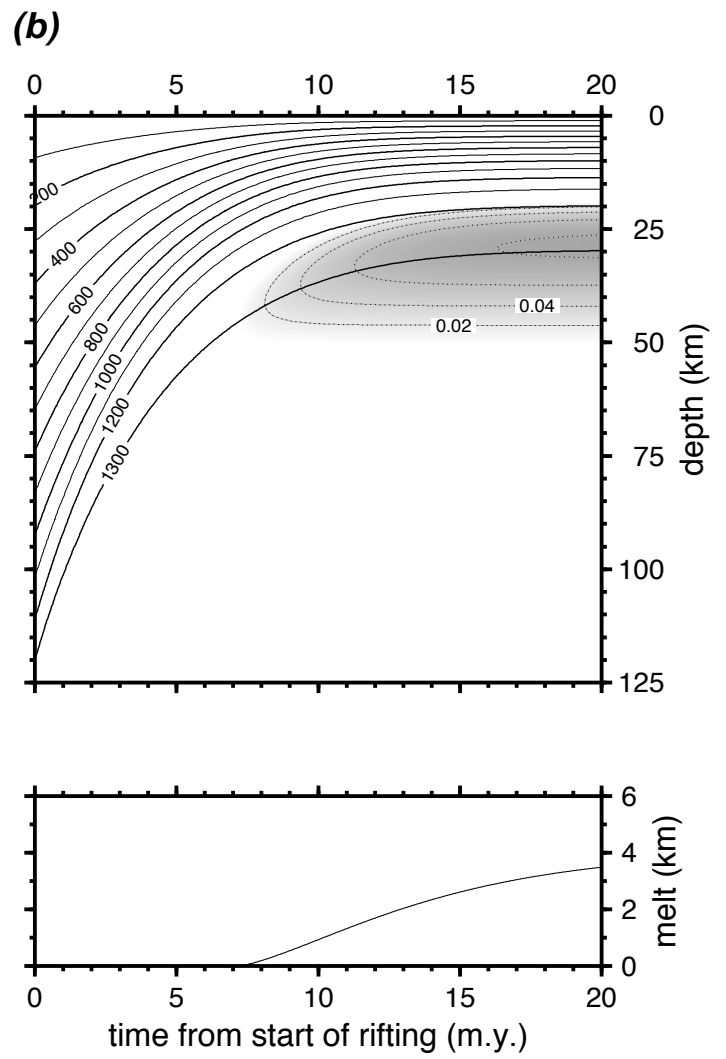
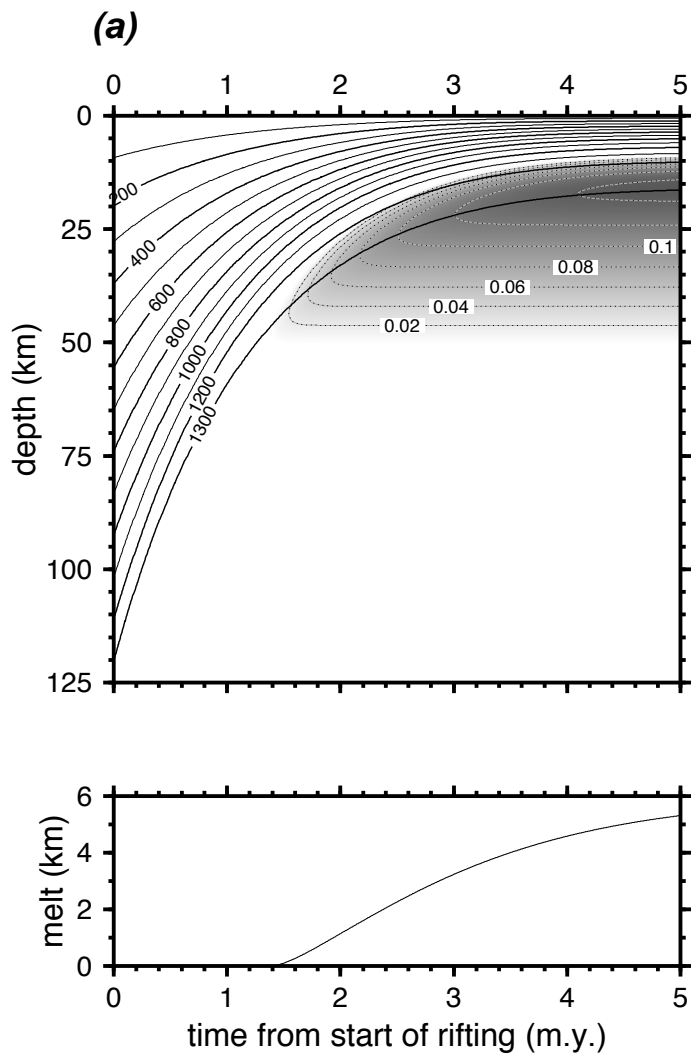


Figure 2
[Click here to download Figure: fig2.eps](#)

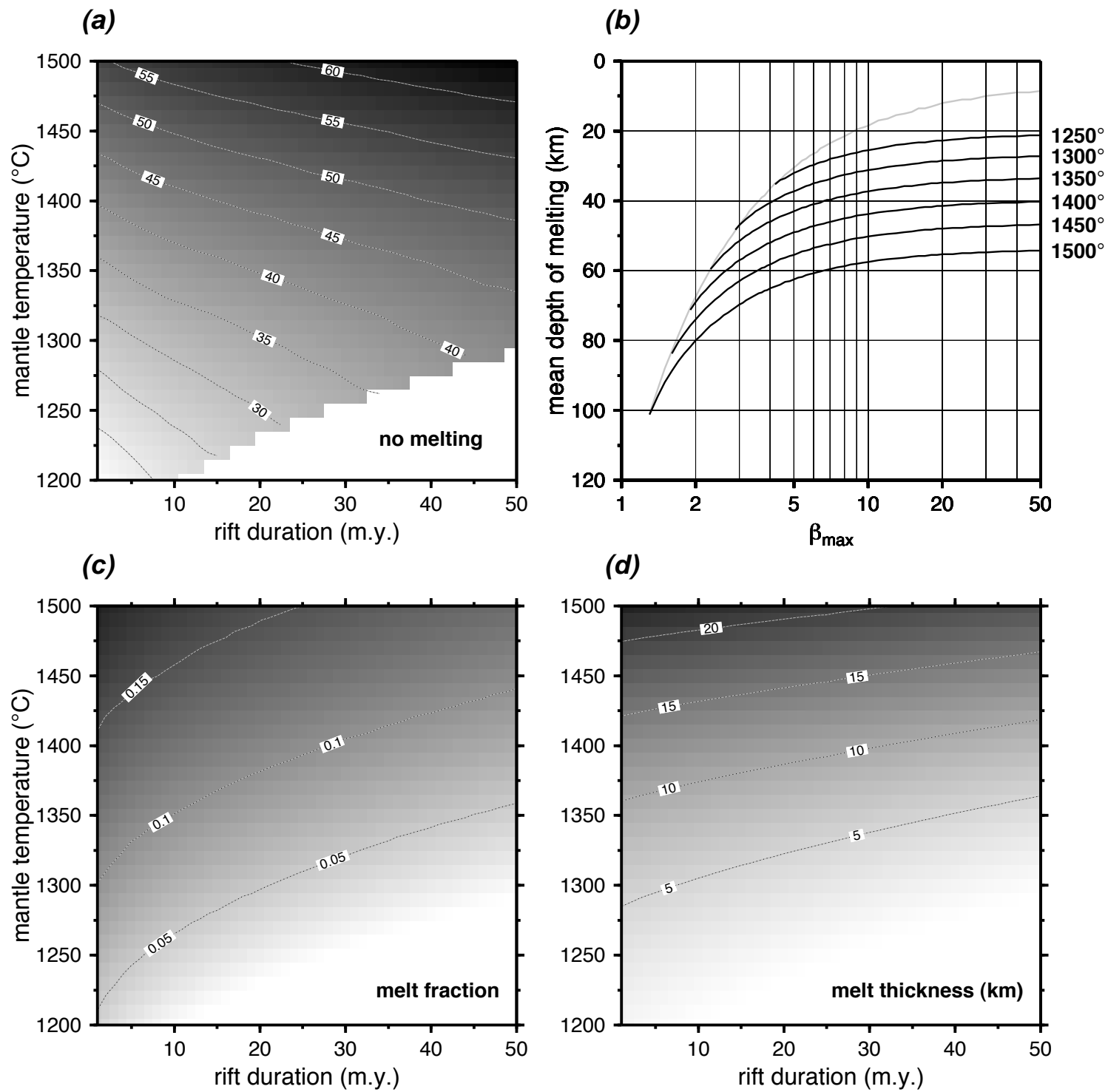


Figure 5
[Click here to download Figure: fig5.eps](#)

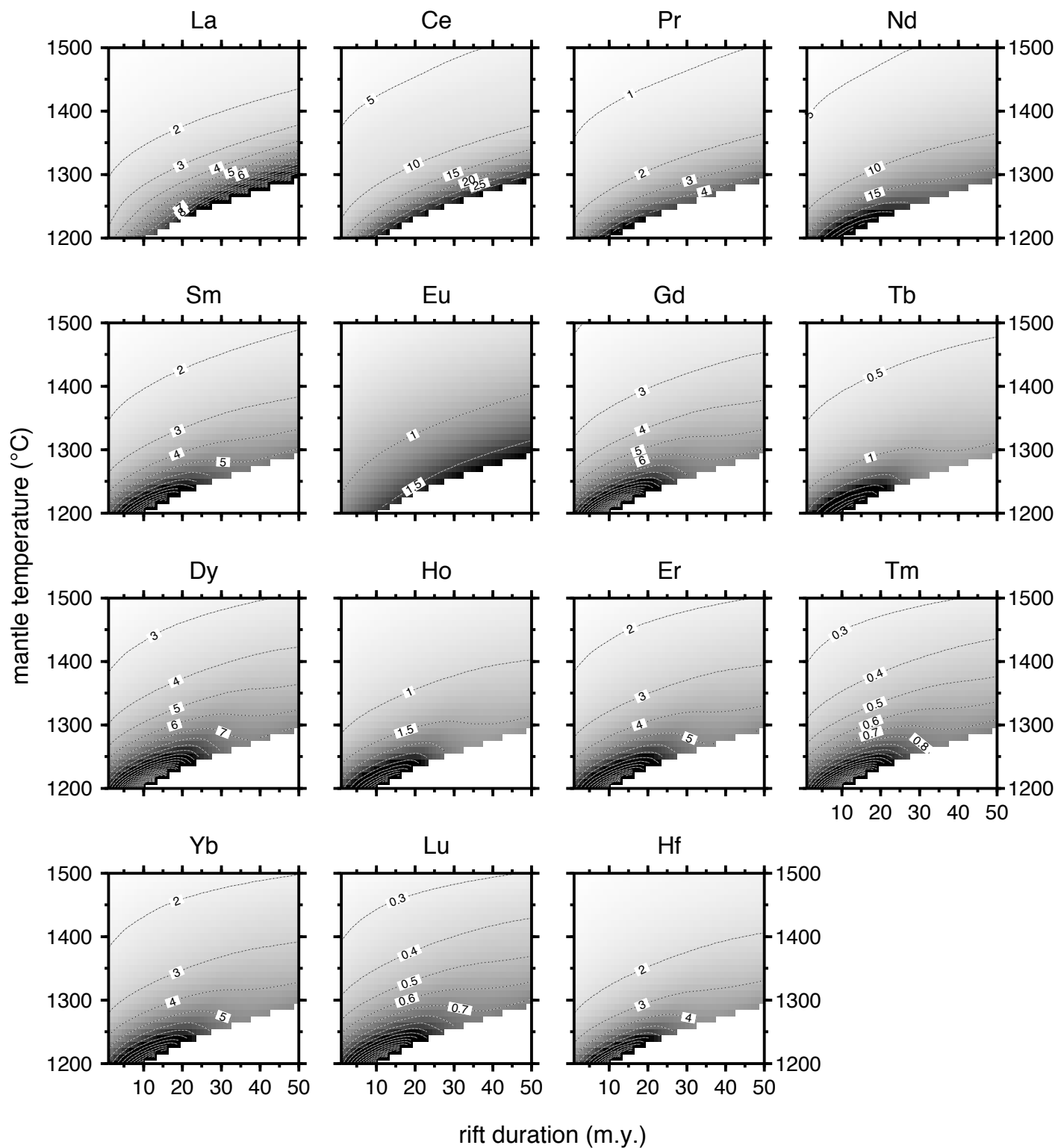


Figure 6

[Click here to download Figure: fig6.eps](#)

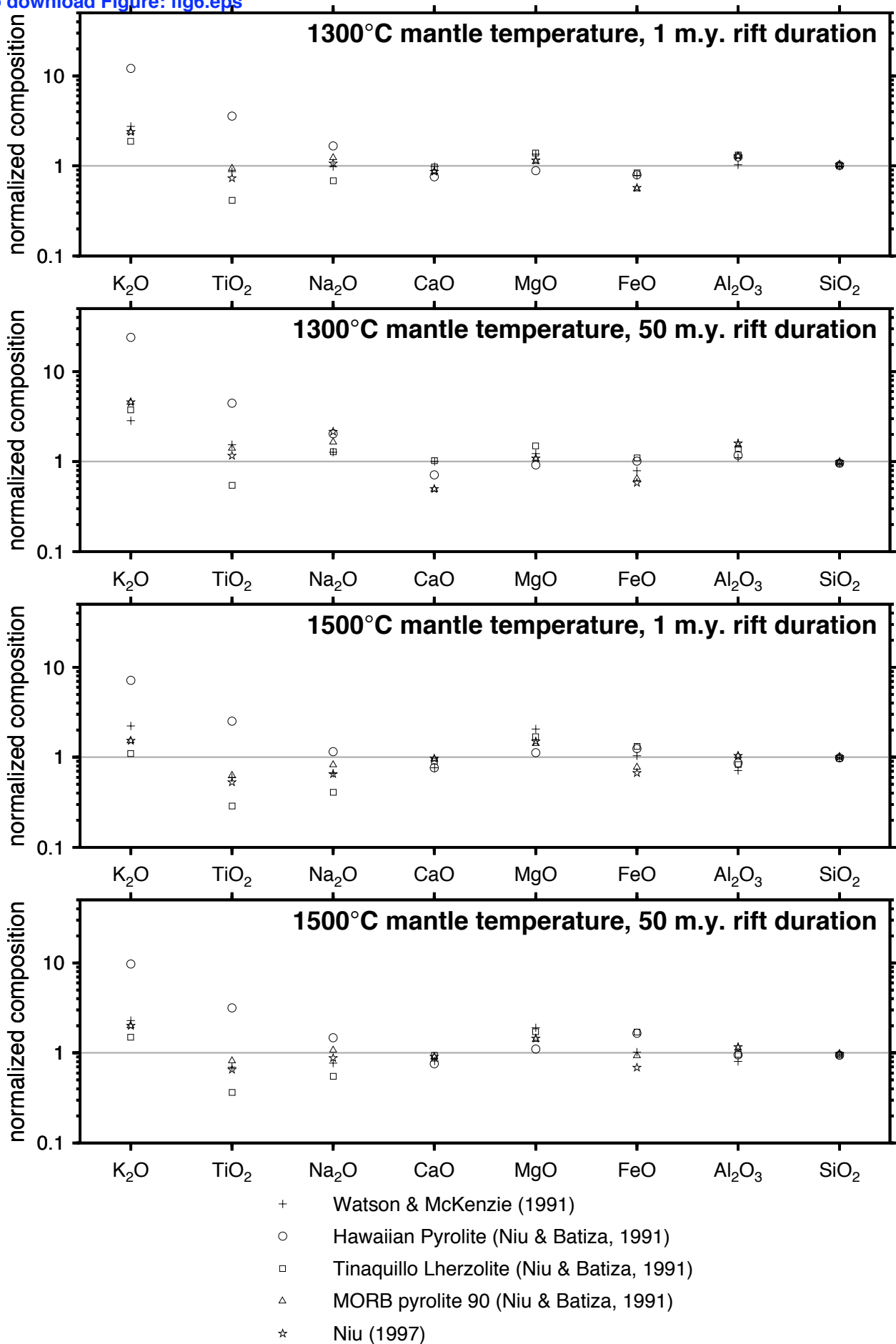


Figure 7

[Click here to download Figure: fig7.eps](#)

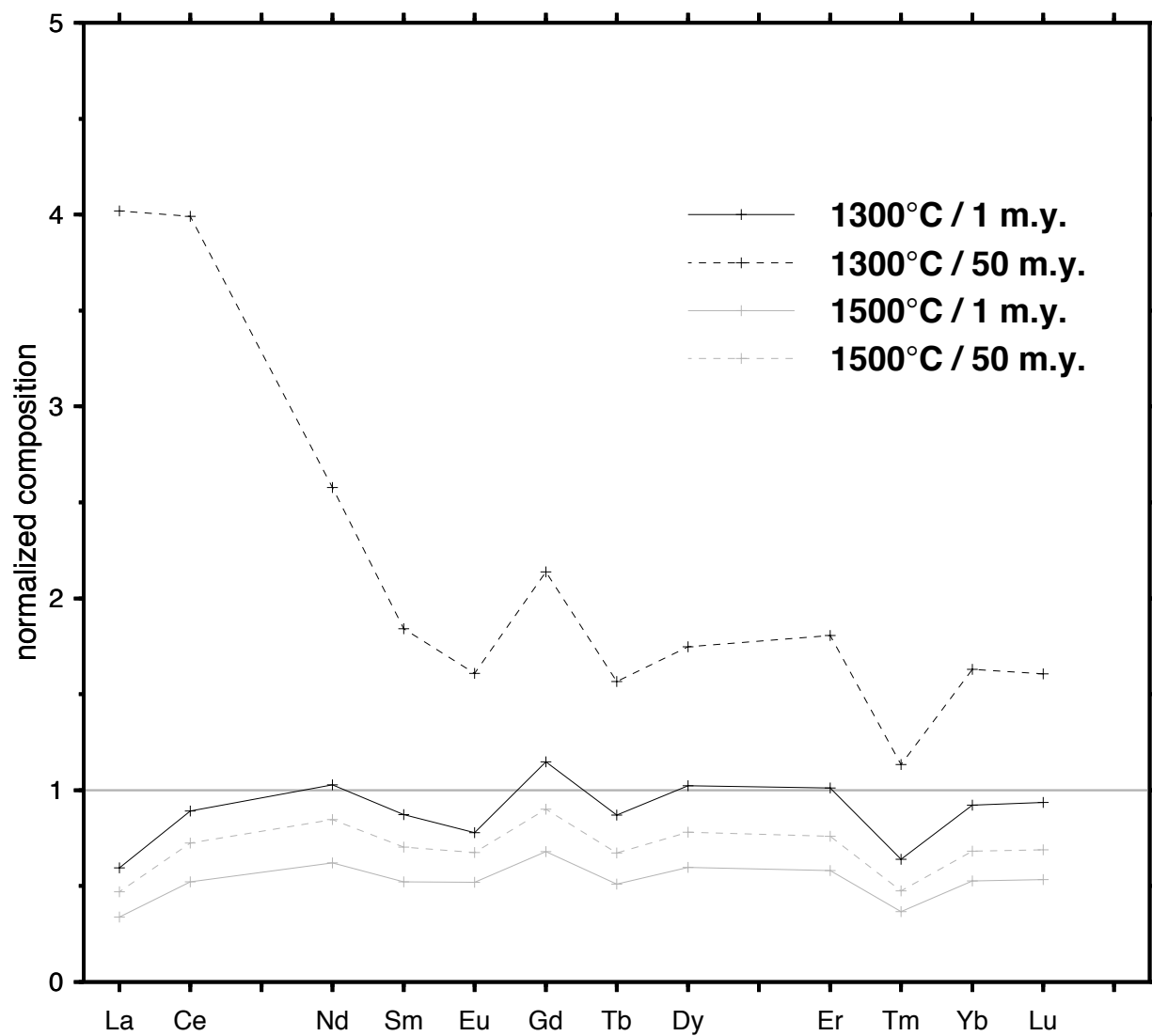


Figure 8

[Click here to download Figure 8 figures](#) Downloaded from [AGU Publications](#) on 09/11/19. See [AGU's Terms and Conditions](#) for more information.

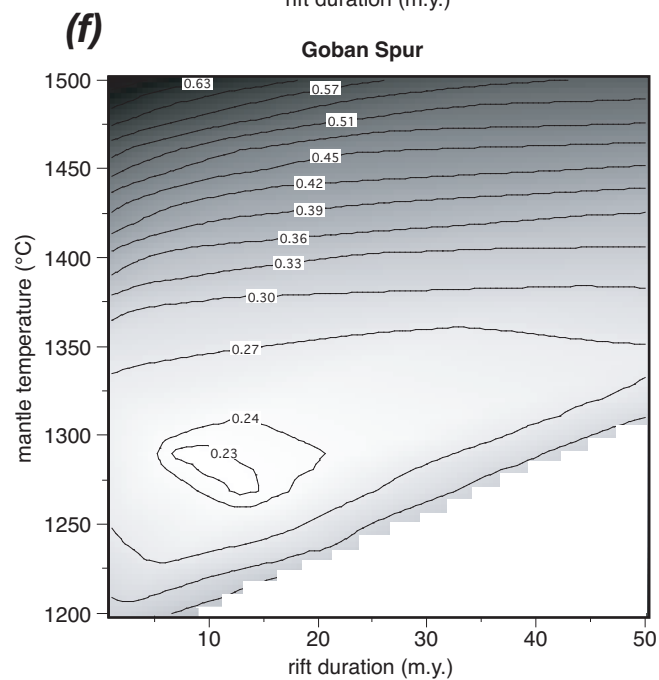
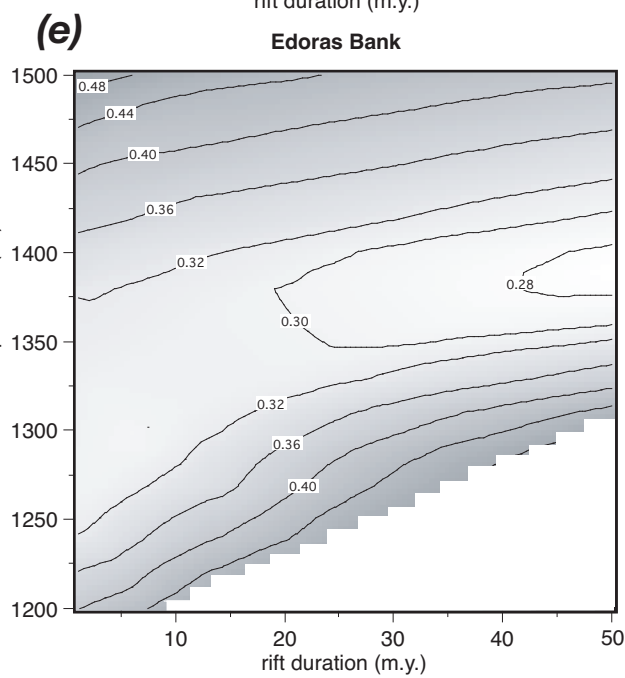
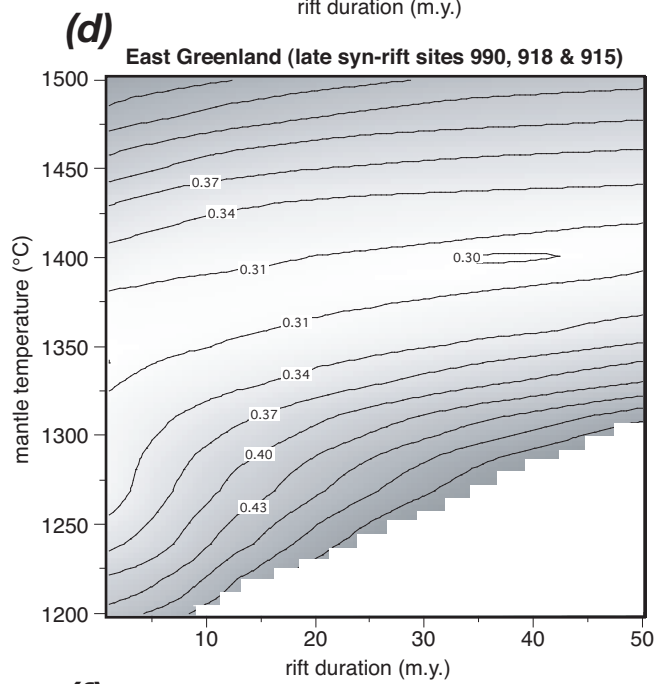
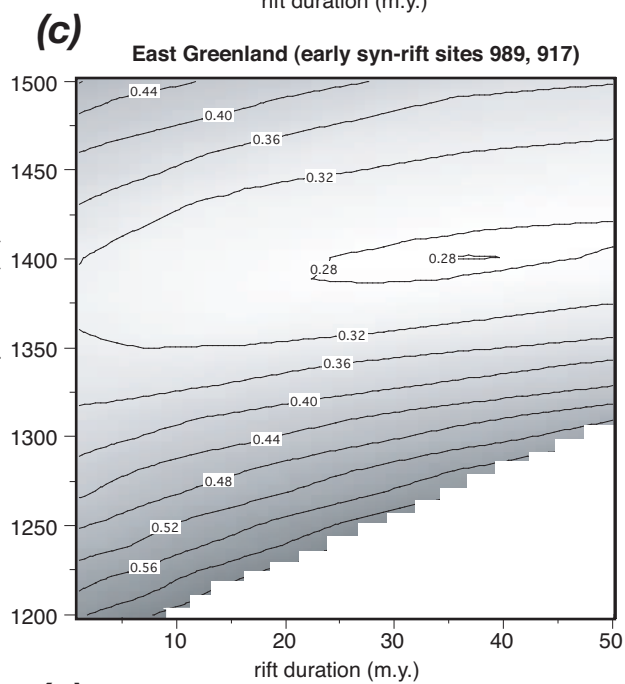
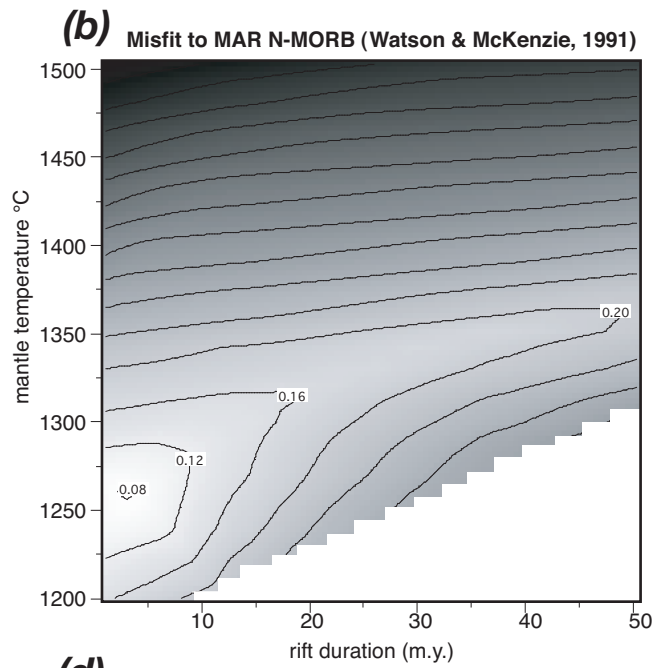
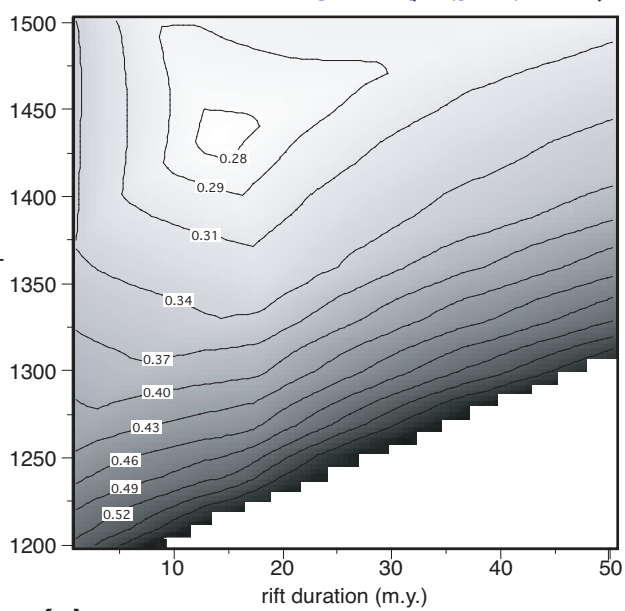


Figure 3

[Click here to download Figure: fig3.eps](#)

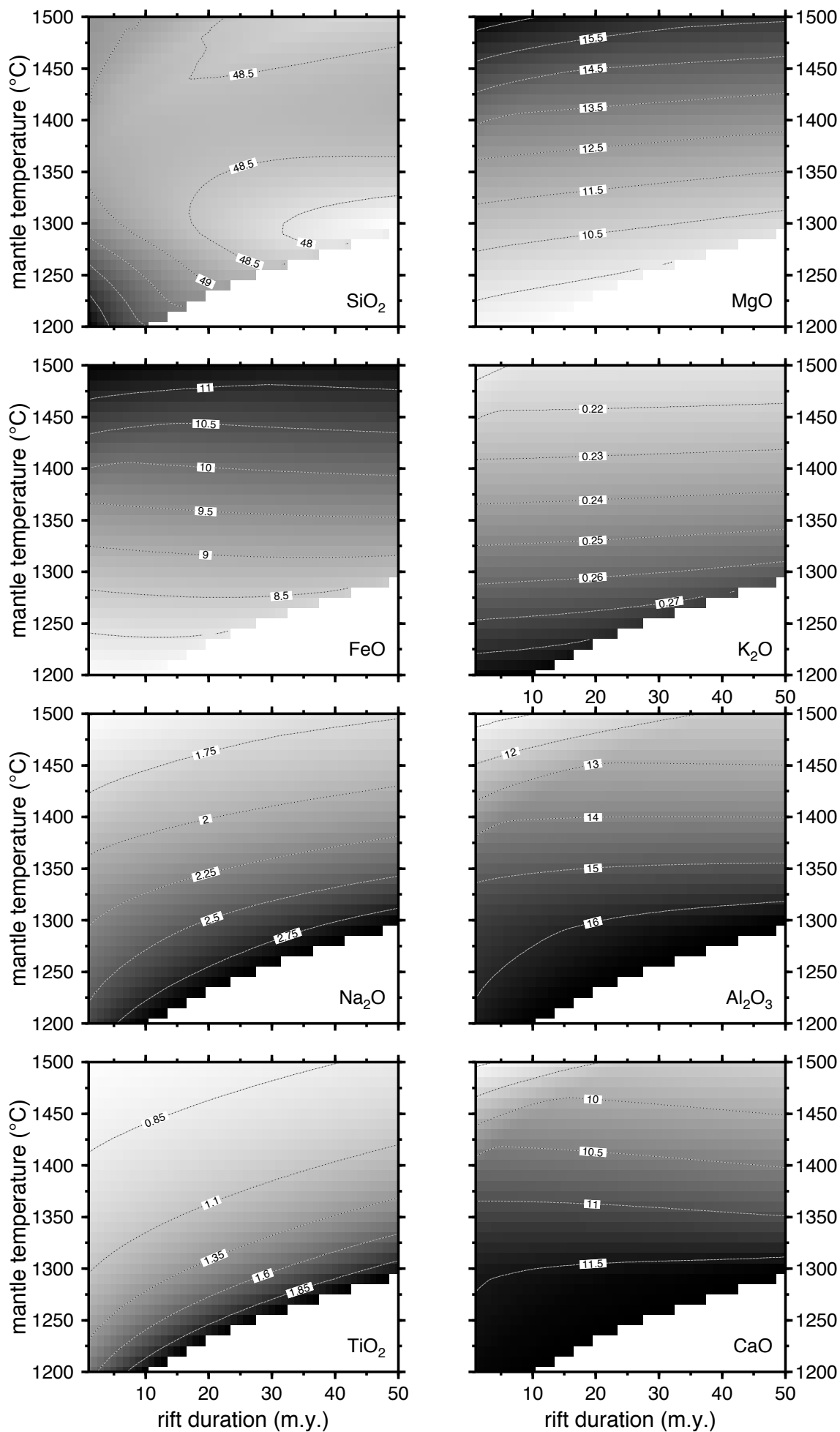
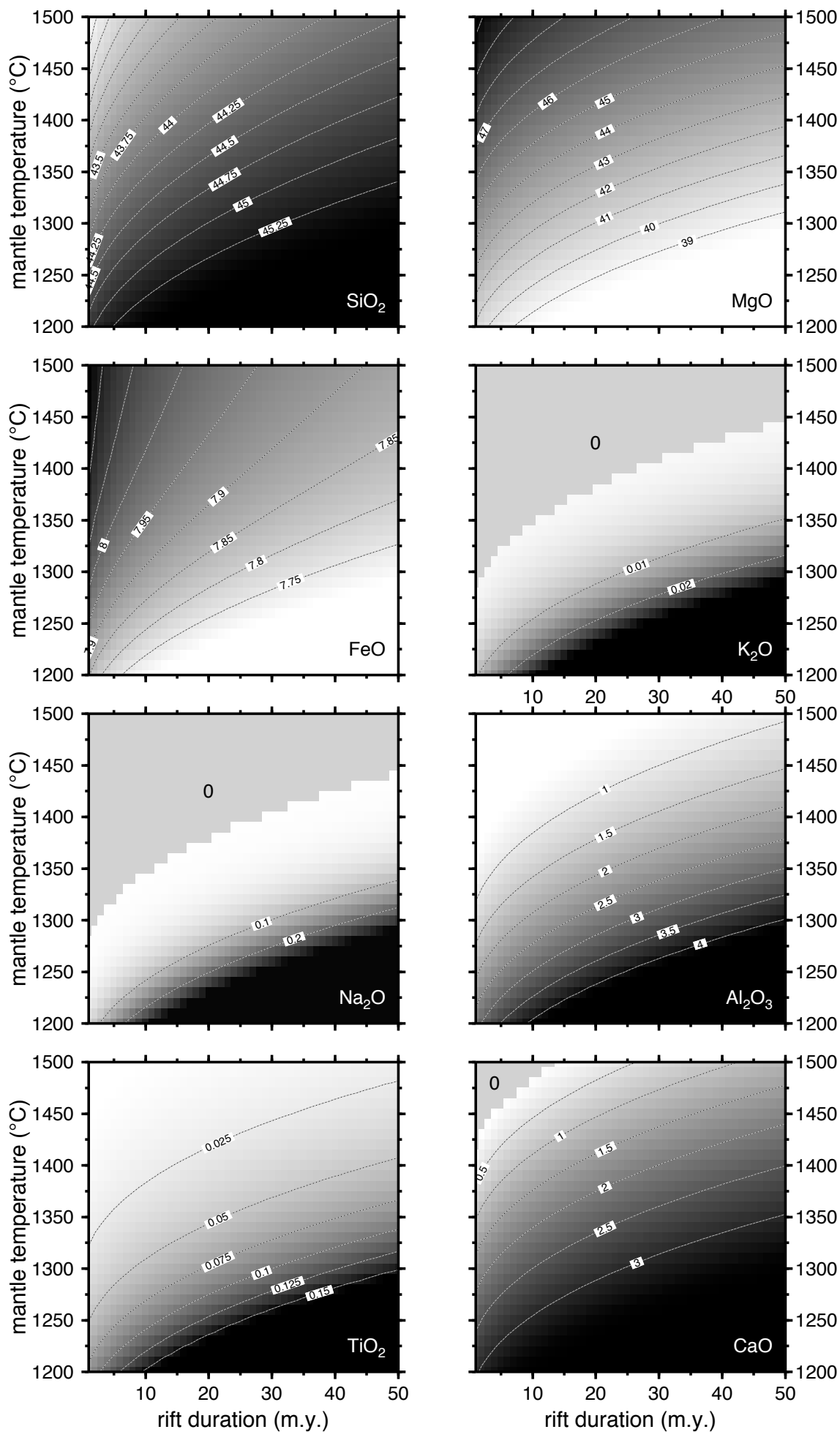


Figure 4

[Click here to download Figure: fig4.eps](#)



Supplementary material for on-line publication only

[Click here to download Supplementary material for on-line publication only: figappendix1.eps](#)

Supplementary material for on-line publication only

[Click here to download Supplementary material for on-line publication only: figappendix2.eps](#)

Supplementary material for on-line publication only

[Click here to download Supplementary material for on-line publication only: figappendix3.eps](#)

Supplementary material for on-line publication only

[Click here to download Supplementary material for on-line publication only: figappendix4.eps](#)

Table 1[Click here to download Table: dean_table1.doc](#)

	SiO ₂	TiO ₂	Al ₂ O ₃	FeO	MgO	CaO	Na ₂ O	K ₂ O
Hawaiian pyrolite	45.20	0.71	3.54	8.47	37.50	3.08	0.57	0.13
Tinaquillo lherzolite	44.95	0.08	3.22	7.66	40.03	2.99	0.18	0.02
MORB pyrolite 90	44.74	0.17	4.37	7.55	38.57	3.38	0.40	0.03
Niu (1997)	45.5	0.16	4.2	7.7	38.33	3.4	0.3	0.03

Table 1: Major element source composition from [20] and [21].

Table 2[Click here to download Table: dean_table2.doc](#)

La	Ce	Pr	Nd	Sm	Eu
0.206±30%	0.722±25%	0.143±20%	0.815±20%	0.299±20%	0.115±15%
Gd	Tb	Dy	Ho	Er	Tm
0.419±15%	0.077±10%	0.525±10%	0.12±10%	0.347±10%	0.054±10%
Yb	Lu	Hf			
0.347±10%	0.054±10%	0.22			

Table 2: Concentration (ppm) of rare earth elements for the depleted Earth source of [22].